

EPIC 218916923b: a low-mass warm Jupiter on a 29-day orbit transiting an active K0 V star

O. Barragán^{1*}, D. Gandolfi¹, A. M. S. Smith², H. J. Deeg^{3,4}, M. C. V. Fridlund^{5,6}, C. M. Persson⁵, P. Donati⁷, M. Endl⁸, Sz. Csizmadia², S. Grziwa⁹, D. Nespral^{3,4}, A. P. Hatzes¹⁰, W. D. Cochran⁸, L. Fossati¹¹, S. S. Brems¹², J. Cabrera², F. Cusano⁷, Ph. Eigmüller¹, C. Eiroa¹³, A. Erikson², E. Guenther¹⁰, J. Korth⁹, L. Mancini^{14,15,16}, M. Pätzold⁹, J. Prieto-Arranz^{3,4}, H. Rauer^{2,17}, I. Rebollido¹³, J. Saario¹⁸ and O. V. Zakhochay^{14,19}

¹Dipartimento di Fisica, Università di Torino, via P. Giuria 1, 10125 Torino, Italy

²Institute of Planetary Research, German Aerospace Center, Rutherfordstrasse 2, 12489 Berlin, Germany

³Instituto de Astrofísica de Canarias, 38205 La Laguna, Tenerife, Spain

⁴Departamento de Astrofísica, Universidad de La Laguna, 38206 La Laguna, Tenerife, Spain

⁵Department of Earth and Space Sciences, Chalmers University of Technology, Onsala Space Observatory, 439 92 Onsala, Sweden

⁶Leiden Observatory, University of Leiden, PO Box 9513, 2300 RA, Leiden, The Netherlands

⁷INAF - Osservatorio Astronomico di Bologna, Via Ranzani, 1, 20127, Bologna, Italy

⁸Department of Astronomy and McDonald Observatory, University of Texas at Austin, 2515 Speedway, Stop C1400, Austin, TX 78712, USA

⁹Rheinisches Institut für Umweltforschung an der Universität zu Köln, Aachener Strasse 209, 50931 Köln, Germany

¹⁰Thüringer Landessternwarte Tautenburg, Sternwarte 5, 07778 Tautenburg, Germany

¹¹Space Research Institute, Austrian Academy of Sciences, Schmiedlstrasse 6, A-8041 Graz, Austria

¹²Landessternwarte, Zentrum für Astronomie der Universität Heidelberg, Königstuhl 12, 69117 Heidelberg, Germany

¹³Departamento Física Teórica, Universidad Autónoma de Madrid, Cantoblanco, 28049 Madrid, Spain

¹⁴Max-Planck-Institut für Astronomie, Königstuhl 17, D-69117 Heidelberg, Germany

¹⁵Department of Physics, University of Rome Tor Vergata, Rome

¹⁶INAF - Astrophysical Observatory of Turin, Turin

¹⁷Center for Astronomy and Astrophysics, TU Berlin, Hardenbergstr. 36, 10623 Berlin, Germany

¹⁸Nordic Optical Telescope, Apartado 474, E-38700 Santa Cruz de La Palma, Spain

¹⁹Main Astronomical Observatory, National Academy of Sciences of the Ukraine, 27 Akademika Zabolotnoho St. 03143, Kyiv, Ukraine

Last updated ; in original form

ABSTRACT

We announce the discovery of EPIC 218916923b, a transiting warm-Jupiter ($T_{\text{eq}}=555\pm 11$ K) on a 29-day orbit around an active ($\log R'_{\text{HK}} = -4.49 \pm 0.03$) K0 V star in K2 Campaign 7. We derive the system's parameters by combining the K2 photometry with ground-based follow-up observations. With a mass of $M_p = 0.381 \pm 0.045 M_{\text{Jup}}$ and radius of $R_p = 0.812 \pm 0.030 R_{\text{Jup}}$, EPIC 218916923b is one of the transiting warm Jupiters with the lowest mass known to date. The planetary mean density $\rho_p = 0.88 \pm 0.14 \text{ g cm}^{-3}$ can be explained with a core of $\sim 50 M_{\oplus}$. Given the brightness of the host star ($V = 11.653$ mag), the relatively short transit duration (~ 5 hours), and the expected amplitude of the Rossiter-McLaughlin effect ($\sim 25 \text{ m s}^{-1}$), EPIC 218916923 is an ideal target to measure the spin-orbit angle of a planetary system hosting a warm Jupiter.

Key words: planetary systems — planets and satellites: detection — planets and satellites: individual: EPIC 218916923 b — stars: fundamental parameters

1 INTRODUCTION

Gas-giant planets ($M_p \gtrsim 0.3 M_{\text{Jup}}$, Hatzes & Rauer 2015) with orbital periods ranging between ~ 10 and 100 days are called warm

* E-mail: oscar.barraganvil@edu.unito.it

Jupiters. They mark the transition between hot Jupiters (giant planets with orbital period between ~ 1 and 10 days) and Jupiter analogues (orbital period longer than 100 days). They seem to be less common than hot Jupiters and their formation scenario is still under debate (e.g., [Frewen & Hansen 2016](#); [Boley et al. 2016](#)). Whereas it is commonly accepted that hot Jupiters did not form *in situ* (e.g., [Kley & Nelson 2012](#)), but rather formed beyond the snow line and then migrated inwards to their current position, it has been recently proposed that warm Jupiters might have formed *in situ* (e.g. [Boley et al. 2016](#); [Huang et al. 2016](#)).

Eighty warm Jupiters have been discovered so far. About thirty are known to transit their parent star and only thirteen have masses and radii known with a precision better than 25 %¹. They have been detected both in low-eccentricity orbits ($e \lesssim 0.4$, e.g., [Brahm et al. 2016](#); [Niedzielski et al. 2016](#); [Smith et al. 2017](#)), as well as in highly eccentric orbits (e.g., [Dawson et al. 2012](#); [Ortiz et al. 2015](#)). [Dong et al. \(2014\)](#) found that warm Jupiters with high eccentricities ($e \gtrsim 0.4$) tend to have a massive planetary/stellar companion in a long period orbit. The architectures of these systems suggest that eccentric warm Jupiters might have reached their current positions via high-eccentricity migration excited by the outer companion ([Dong et al. 2014](#)). On the other hand, warm Jupiters with no detected Jovian companion tend to have lower eccentricities peaked around 0.2. This suggests that two different types of warm Jupiters might exist: those formed via high-eccentricity migration and those formed *in situ*. Alternatively, warm Jupiters in low-eccentricity orbits can also result from disc-driven migration from the outer region of the system ([Kley & Nelson 2012](#)).

[Petrovich & Tremaine \(2016\)](#) studied the possibility that warm Jupiters are undergoing secular eccentricity oscillations induced by an outer companion in an eccentric and/or mutually inclined orbit. Their model suggests that high-eccentricity migration can account for most of the hot Jupiters, as well as for most of the warm Jupiters with $e \gtrsim 0.4$. However, it cannot account for the remaining population of low-eccentricity warm Jupiters, which must have undergone a different formation mechanism. The low efficiency to generate warm Jupiters in nearly circular orbits via high-eccentricity migration has been corroborated by [Hamers et al. \(2016\)](#) and [Antonini et al. \(2016\)](#) using numerical simulations.

In order to test different planet formation mechanisms, we need to characterize the population of warm Jupiters in terms of planetary mass, radius and orbital parameters. From this point of view, space-based transit surveys are uniquely able to uncover the properties of long-period planets, thanks to the continuous high-precision photometric monitoring only achievable from space.

We herein present the discovery of EPIC 218916923b, a transiting warm Jupiter ($M_p = 0.381 \pm 0.045 M_{\text{Jup}}$, $R_p = 0.812 \pm 0.030 R_{\text{Jup}}$) in a 29-day orbit around an active K0 V star that has been photometrically monitored by the *K2* space-mission during its Campaign 7. We combine the *K2* photometry with ground-based imaging and high-precision radial velocity measurements to confirm the planet and derive the main parameters of the system.

2 K2 PHOTOMETRY

K2 Campaign 7 was performed between 2015 October 04 UT and 2015 December 26 UT². The *Kepler* spacecraft was pointed at co-

Table 1. Main identifiers, coordinates, optical and infrared magnitudes, and proper motion of C7_6923.

Parameter	Value	Source
<i>Main Identifiers</i>		
TYC	6300-2008-1	Tycho
EPIC	218916923	EPIC
UCAC	361-185490	EPIC
2MASS	19161596-1754384	EPIC
<i>Equatorial coordinates</i>		
α (J2000.0)	19 ^h 16 ^m 15.967 ^s	2MASS
δ (J2000.0)	-17°54′38.48″	2MASS
<i>Magnitudes</i>		
<i>B</i>	12.433±0.205	EPIC
<i>V</i>	11.653±0.137	EPIC
<i>g</i>	12.049±0.010	EPIC
<i>r</i>	11.400±0.010	EPIC
<i>J</i>	10.177±0.022	2MASS
<i>H</i>	9.768±0.022	2MASS
<i>K</i>	9.660±0.023	2MASS
W1	9.598±0.024	WISE
W2	9.684±0.020	WISE
W3	9.593±0.043	WISE
W4	8.487	WISE
<i>Proper motions</i>		
$\mu_\alpha \cos \delta$ (mas yr ⁻¹)	38.584 ± 3.907	Gaia
μ_δ (mas yr ⁻¹)	-9.837 ± 3.534	Gaia

Note – Values of fields marked with EPIC are taken from the Ecliptic Plane Input Catalog, available at <http://archive.stsci.edu/k2/epic/search.php>. Values marked with Gaia, 2MASS, and WISE are from [Fabricius et al. \(2016\)](#), [Cutri et al. \(2003\)](#), and [Cutri et al. \(2012\)](#), respectively. The WISE W4 magnitude is an upper limit.

ordinates $\alpha = 19^{\text{h}}11^{\text{m}}19^{\text{s}}$, $\delta = -23^{\circ}21'36''$. *K2* observed simultaneously 13 469 sources in long cadence mode (~ 30 minute integration time) and 72 objects in short cadence mode (~ 1 minute integration time), leading to a total of 13 541 light curves.

For the detection of transiting planet candidates, we used the *K2* Campaign 7 light curves³ extracted by [Vanderburg & Johnson \(2014\)](#). We analyzed the light curves using the DST algorithm ([Cabrera et al. 2012](#)) and the EXOTRANS pipeline ([Grziwa et al. 2012](#); [Grziwa & Pätzold 2016](#)). Both codes have been used extensively on *CoRoT* ([Carpano et al. 2009](#); [Cabrera et al. 2009](#); [Erikson et al. 2012](#); [Carone et al. 2012](#); [Cavarroc et al. 2012](#)) and *Kepler* ([Cabrera et al. 2014](#); [Grziwa & Pätzold 2016](#)) data. These search algorithms detect periodic patterns in time series photometric data. DST uses an optimized transit shape with the same number of free parameters as for the BLS algorithm (Box-fitting Least Squares; [Kovács et al. 2002](#)), and it also implements better statistics for signal detection. EXOTRANS uses the BLS algorithm combined with the wavelet-based filter technique VARLET ([Grziwa & Pätzold 2016](#)), diminishing the effects of stellar variability and data discontinuities.

¹ Source: <http://exoplanet.eu>, as of January 2017.

² See <http://keplerscience.arc.nasa.gov/k2-fields.html>.

³ Publicly available at <https://www.cfa.harvard.edu/~avanderb/allk2c7obs.html>.

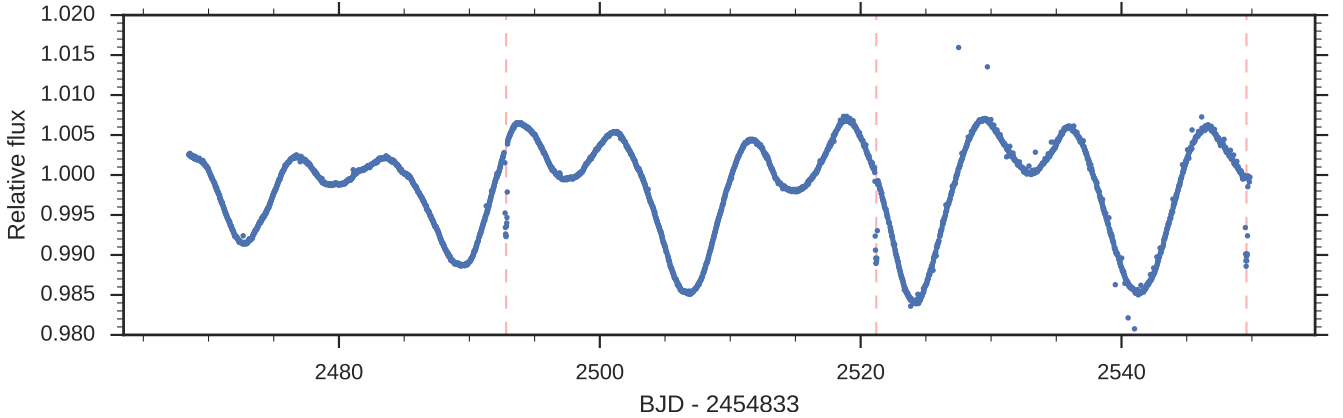


Figure 1. K2 Light curve for C7_6923 as extracted by Luger et al. (2016). The positions of the 3 observed transits are marked with vertical dashed lines.

We detected a periodic transit-like signal associated with the star EPIC 218916923 with both DST and EXOTRANS. As a sanity check, we downloaded the EVEREST light curve of EPIC 218916923 (Luger et al. 2016) and detected the same signal. We note that Vanderburg & Johnson (2014) and Luger et al. (2016) used the same mask to extract the times-series data from the raw K2 images. EPIC 218916923 was proposed for K2 observations by programs GO7086 (P.I. Thompson), GO7030 (P.I. Howard) and GO7087 (P.I. Dragomir). We will hereafter refer to the star and its transiting planet as C7_6923 and C7_6923b, respectively.

We searched the light curve of C7_6923 for odd-even transit depth variations, deep secondary eclipse, and large photometric variations in phase with the candidate orbital period that might unveil the presence of an eclipsing binary making the system a likely false positive. None of them were found. We proceeded to more detailed fitting of the light curve, as well as ground-based imaging (Sect. 3) and spectroscopic observations (Sect. 4). The main identifiers, coordinates, optical and infrared magnitudes, and proper motions of the star are listed in Table 1. We display the EVEREST K2 light curve of C7_6923 in Fig. 1.

3 ALFOSC IMAGING

K2 Campaign 7 is projected close to the galactic center and thus in a relatively crowded stellar region. In order to estimate the contamination factor arising from sources whose light leaks into the photometric masks used by Vanderburg & Johnson (2014) and Luger et al. (2016), we observed C7_6923 on 13 September 2016 (UT) with the ALFOSC camera mounted at the Nordic Optical Telescope (NOT) of Roque de los Muchachos Observatory (La Palma, Spain). The sky conditions were photometric with excellent seeing. We used the Bessel R-filter and acquired 16 images of 6 sec, 2 images of 20 sec, and 1 image of 120 sec. The data were bias subtracted and flat-fielded using dusk sky flats. Aperture photometry was then performed on all stars within the mask used in the extraction of the light curve by Vanderburg & Johnson (2014) and Luger et al. (2016).

Several faint stars can be identified inside the photometric mask (Fig. 2), of which the two brightest sources are also in the EPIC catalog with Kepler band magnitudes of 16.8 and 18.4. The closest detected source is a 6.8-mag fainter star at 3.8'' South of C7_6923. We can exclude close stars as faint as ~ 20 mag anywhere

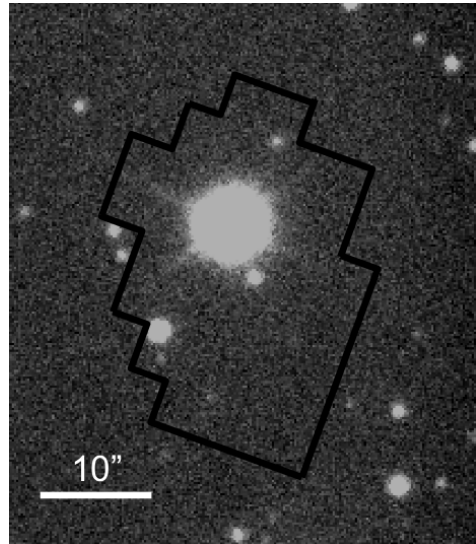


Figure 2. ALFOSC Bessel R-band image of the sky region around C7_6923. The target star is the brightest source in the middle. The solid black polygon marks the EVEREST photometric mask (Luger et al. 2016).

else outside the ALFOSC PSF of 0.6'' FWHM. It is worth noting that the faintest star whose flux could account for the $\sim 1\%$ deep transit of C7_6923 cannot be more than ~ 5 mag fainter than our target. The summed flux of these faint stars amounts to $1.4 \pm 0.3\%$ of the total off-transit flux within the aperture. We subtracted the contamination flux from the EVEREST K2 light curve prior to performing the joint analysis presented in Sect. 6.

4 HIGH-RESOLUTION SPECTROSCOPY

In June and August 2016 we obtained two reconnaissance spectra of C7_6923 with the Tull spectrograph (Tull et al. 1995) at the 2.7-m telescope at McDonald Observatory (Texas, USA). The high resolution ($R \approx 60\,000$) spectra have a signal-to-noise ratio of ~ 30 per pixel at 5500Å. We reduced the data using standard IRAF routines and derived preliminary spectroscopic parameters using our code Kea (Endl & Cochran 2016). The results from both spectra are nearly identical and reveal a star with $T_{\text{eff}} = 5500 \pm 100$ K,

$\log g_\star = 4.65 \pm 0.12$ (cgs), $[\text{Fe}/\text{H}] = +0.11 \pm 0.12$ dex, and a slow projected rotational velocity of $v \sin i_\star \approx 2 \text{ km s}^{-1}$.

The high-precision radial velocity follow-up of C7_6923 was started in June 2016 with the FIBre-fed Échelle Spectrograph (FIES; Frandsen & Lindberg 1999; Telting et al. 2014) mounted at the 2.56-m Nordic Optical Telescope (NOT). The observations were carried out as part of the OPTICON and CAT observing programs 16A/055, P53-201, and P53-203. We used the *high-res* mode, which provides a resolving power of $R \approx 67\,000$ in the whole visible spectral range. Following the observing strategy outlined in Buchhave et al. (2010) and Gandolfi et al. (2015), we traced the RV drift of the instrument by acquiring long-exposed ($T_{\text{exp}} \approx 35$ sec) ThAr spectra immediately before and after the target observations. The exposure time was set to 2100–3600 sec, based on sky conditions and observing scheduling constraints. The data reduction uses standard IRAF and IDL routines. The signal-to-noise ratio (SNR) of the extracted spectra is ~ 30 – 40 per pixel at 5500 \AA . Radial velocity measurements were extracted via multi-order cross-correlation with the RV standard star HD 182572, observed with the same instrument set-up as C7_6923.

We also observed C7_6923 in July, August, and September 2016 with the HARPS (Mayor et al. 2003) and HARPS-N (Cosentino et al. 2012) spectrographs mounted at the ESO 3.6-m Telescope of La Silla Observatory (Chile) and at the 3.58-m Telescopio Nazionale Galileo (TNG), of Roque de los Muchachos observatory (La Palma, Spain), respectively. Both instruments provide a resolving power of $R \approx 115\,000$ in the wavelength range ~ 3800 – 6900 \AA . The observations were performed as part of the ESO and TNG observing programs 097.C-0948 and A33TAC_15, respectively. The exposure time was set to 1800 sec, leading to a SNR of ~ 35 on the extracted spectra. We reduced the data using the dedicated HARPS and HARPS-N pipelines and extracted the RVs by cross-correlation with a G2 numerical mask.

The FIES, HARPS, and HARPS-N RVs are listed in Table 2 along with the bisector span (BIS) of the cross-correlation function (CCF). The time stamps are given in barycentric Julian date in barycentric dynamical time (BJD_{TDB}). The RVs shows no significant correlation with the BIS measurements. The linear Pearson correlation coefficients is -0.01 with a p-value of 0.97 . This supports the fact that the observed RV variation is induced by the orbiting planet.

5 STELLAR PARAMETERS

5.1 Spectral analysis

We derived the spectroscopic parameters of C7_6923 from the co-added FIES spectra. The stacked FIES data have a SNR of ~ 110 per pixel at 5500 \AA . We adopted three different methods. For each the method, results are reported in Table 3.

First method. The technique uses ATLAS 9 model spectra (Castelli & Kurucz 2004) to fit spectral features that are sensitive to different photospheric parameters. Microturbulent (v_{mic}) and macroturbulent (v_{mac}) velocities are derived from the calibration equations of Bruntt et al. (2010) and Doyle et al. (2014). We used the wings of the H_α and H_β lines to estimate the effective temperature (T_{eff}), and the $\text{Mg I } 5167$, 5173 , and 5184 \AA , $\text{Ca I } 6162$ and 6439 \AA , and the Na I D lines to determine the surface gravity $\log g_\star$. We simultaneously fitted different spectral regions to measure the iron abundance $[\text{Fe}/\text{H}]$. The projected rotational velocity $v \sin i_\star$ was determined by fitting the profile of many isolated and unblended metal lines.

Table 2. Radial velocity measurements of C7_6923.

BJD_{TDB}	RV (km s^{-1})	σ_{RV} (km s^{-1})	CCF BIS (km s^{-1})
FIES			
7565.656116	−31.3755	0.0160	0.0119
7568.556388	−31.3503	0.0155	0.0129
7569.567239	−31.3317	0.0153	0.0264
7570.606019	−31.3473	0.0136	0.0098
7572.576513	−31.3357	0.0133	0.0107
7574.529831	−31.3466	0.0101	0.0072
7576.536114	−31.2990	0.0136	0.0016
7579.547224	−31.3441	0.0139	−0.0015
7585.551244	−31.3706	0.0111	0.0084
7589.540362	−31.3913	0.0143	0.0130
HARPS			
7569.713312	−31.1633	0.0032	0.0144
7587.829506	−31.2146	0.0052	0.0142
7589.522953	−31.2116	0.0049	0.0131
7610.717148	−31.2217	0.0028	0.0045
7619.530966	−31.2190	0.0031	−0.0146
7620.681855	−31.2049	0.0069	0.0069
HARPS-N			
7586.621003	−31.2048	0.0029	0.0103
7587.602796	−31.2141	0.0038	0.0072
7605.428985	−31.1683	0.0050	−0.0003

Second method. It relies on the use of the spectral analysis package Spectroscopy Made Easy (SME; Valenti & Piskunov 1996; Valenti & Fischer 2005). For a set of given stellar parameters, SME calculates synthetic spectra of stars and fits them to observed high-resolution spectra using a chi-squared minimization procedure. We used SME version 4.4.3 and ATLAS 12 model spectra (Kurucz 2013). We adopted the same calibration equation as described in the first method to estimate v_{mic} and v_{mac} . The fitted spectral features are the same as in the previous paragraph.

Third method. It uses the classical equivalent width (EW) method adopting the following criteria: *i*) T_{eff} is obtained by removing trends between abundance of the chemical elements and the respective excitation potentials; *ii*) $\log g_\star$ is optimised by assuming the ionisation equilibrium condition, i.e., by requiring that for a given species, the same abundance (within the uncertainties) is obtained from lines of two ionisation states (typically, neutral and singly ionised lines); *iii*) v_{mic} is set by minimising the slope of the relationship between abundance and the logarithm of the reduced EWs. The equivalent widths of Fe I and Fe II lines are measured using the code DOOp (Cantat-Gaudin et al. 2014), a wrapper of DAOSPEC (Stetson & Pancino 2008). The stellar atmosphere parameters are derived with the program FAMA (Magrini et al. 2013), a wrapper of MOOG (Snedden et al. 2012). We used the public version of the atomic data prepared for the *Gaia*-ESO Survey (Heiter et al. 2015) and based on the VALD3 data (Ryabchikova et al. 2011). We used ~ 200 Fe I lines and ~ 10 Fe II lines for the determination of the stellar parameters.

The final adopted estimates are the error-weighted mean values of the three methods and are listed in Table 4. We obtained $T_{\text{eff}} = 5287 \pm 60 \text{ K}$, $\log g_\star = 4.52 \pm 0.06$ (cgs), $[\text{Fe}/\text{H}] = 0.21 \pm 0.05$ dex, $v_{\text{mic}} = 0.87 \pm 0.06 \text{ km s}^{-1}$, $v_{\text{mac}} = 2.44 \pm 0.38 \text{ km s}^{-1}$ and $v \sin i_\star = 2.91 \pm 0.38 \text{ km s}^{-1}$. Using the Pecaut & Mamajek (2013)’s calibration scale for dwarf

Table 3. Spectroscopic parameters of C7_6923 as derived using the three methods described in Sect 5.

Method	T_{eff} (K)	$\log g_{\star}$ (cgs)	[Fe/H] (dex)	v_{mic} (km s $^{-1}$)	v_{mac} (km s $^{-1}$)	$v \sin i_{\star}$ (km s $^{-1}$)
Method 1	5340±110	4.50±0.09	0.22±0.08	0.9±0.1	2.5±0.6	2.8±0.6
Method 2	5185±100	4.53±0.10	0.20±0.10	0.8±0.1	2.4±0.5	3.0±0.5
Method 3	5343±99	4.58±0.21	0.21±0.10	0.9±0.1	–	–

stars, the effective temperature of C7_6923 defines the spectral type of the host star as K0 V.

5.2 Interstellar extinction

We measured the visual reddening (A_V) of C7_6923 following the technique described in [Gandolfi et al. \(2008\)](#). We fitted the spectral energy distribution of the star to synthetic colors extracted from the BT-NEXTGEN model spectrum ([Allard et al. 2011](#)) with the same photospheric parameters as the star. We adopted the extinction law of [Cardelli et al. \(1989\)](#) and assumed a normal value for the total-to-selective extinction ($R_V = A_V/E(B-V) = 3.1$). We measured a visual extinction of $A_V = 0.05 \pm 0.05$ mag. This value is below the upper limit of $A_V \leq 0.3$ mag extracted from the [Schlegel et al. \(1998\)](#)'s all-sky extinction map, corroborating our result.

5.3 Rotational period

The *K2* light curve of C7_6923 displays periodic and quasi-periodic variations with a peak-to-peak photometric amplitude of $\sim 2\%$ (Fig. 1). The late-type spectral type of the star suggests that the observed variability is due to Sun-like spots appearing and disappearing from the visible stellar disc as the star rotates around its axis. This is corroborated by the fact that the C7_6923 is a chromospherically active star. The FIES, HARPS, and HARPS-N shows clear emission components in the cores of the Ca II H&K lines, from which we estimated the average Mt. Wilson indices⁴ of $S_{\text{HK}} = 0.37 \pm 0.02$ and $\log R'_{\text{HK}} = -4.49 \pm 0.03$.

The out-of-transit photometric variability observed in the light curve of C7_6923 is mainly due to two active regions located at opposite stellar longitudes, whose lifetime is longer than the duration of the *K2* observations. Using the spots as tracers of stellar rotation and following the auto correlation function (ACF) technique described in [McQuillan et al. \(2014\)](#), we estimated that the rotational period of the star is $P_{\text{rot}} = 17.24 \pm 0.12$ days. The Lomb-Scargle periodogram of the light curve shows its strongest peak at the same period confirming our results.

5.4 Stellar mass, radius and age

We derived the stellar mass, radius, and age using the online interface for Bayesian estimation of stellar parameters available at the following web page: <http://stev.oapd.inaf.it/cgi-bin/>

⁴ The reported indices are corrected for the the interstellar medium absorption, following the procedure described in [Fossati et al. \(2017\)](#) and using the measured stellar parameters and reddening. The corrections are 0.04 and 0.06 for S_{HK} and $\log R'_{\text{HK}}$, respectively. The star is therefore slightly more active than what measured from the spectra.

[param](#). Following [da Silva et al. \(2006\)](#), the web tool interpolates onto PARSEC model isochrones ([Bressan et al. 2012](#)) the V-magnitude (Table 1) - which we corrected for the interstellar extinction derived in Sect 5.2 - parallax - as extracted from the *Gaia*'s first data release ($px = 6.56 \pm 0.43$ mas, $d = 152 \pm 10$ pc [Fabricius et al. 2016](#)) - the metal content and effective temperature - see Sect. 5. We adopted the log-normal initial mass function from [Chabrier \(2001\)](#).

C7_6923 has a mass of $M_{\star} = 0.918 \pm 0.028 M_{\odot}$ and radius of $R_{\star} = 0.860 \pm 0.031 R_{\odot}$, corresponding to a surface gravity of $\log g_{\star} = 4.504 \pm 0.035$ (cgs), in excellent agreement with the spectroscopically derived value of $\log g_{\star} = 4.52 \pm 0.06$ (cgs; see Sect. 5). The derived mean density $\rho_{\star} = 2.04^{+0.24}_{-0.21}$ g cm $^{-3}$ of C7_6923 is also consistent within 1- σ with the density estimated by the modeling of the transit light curve ($\rho_{\star} = 2.19 \pm 0.20$ g cm $^{-3}$; see Sect. 6).

The isochrones provide a poorly constrained age of 3.6 ± 3.4 Gyr for C7_6923. Using the equations given in [Barnes & Kim \(2010\)](#) and [Barnes \(2010\)](#), the rotation period of 17.3 days (Sect 5.3) implies a gyrochronological age of 1.8 ± 0.3 Gyr.

6 JOINT RV-TRANSIT FIT

We performed the joint fit to the photometric and RV data using the code `pyaneti`, a Python/Fortran software suite based on Markov Chain Monte Carlo (MCMC) methods ([Barragán et al.](#), in preparation).

The photometric data included in the joint analysis are subsets of the whole EVEREST *K2* light curve. We used the EVEREST light curve because it provides a slightly better rms over the [Vanderburg & Johnson \(2014\)](#)'s data. We selected ~ 10 hours of data-points around each of the 3 transits, which have a duration of ~ 5 hours. We de-trended the individual transits using a second-order polynomial fitted to the out-of-transit points. The fitted data include 12 points immediately before and after each transit, with the exception of the last transit for which only 9 data points are available. We removed the data points that are affected by stellar spot crossing events (see Sect. 7.1 for more details).

We used a Keplerian orbit for the RV data and a quadratic law of [Mandel & Agol \(2002\)](#) for the transit model. We adopted the Gaussian likelihood

$$\mathcal{L} = \left[\prod_{i=1}^{n_{\text{rv}}} \{2\pi(\sigma_i^2 + \sigma_j^2)\}^{-1/2} \right] \exp \left\{ - \sum_{i=1}^{n_{\text{rv}}} \frac{(D_i - M_i)^2}{2(\sigma_i^2 + \sigma_j^2)} \right\} \times \left[\prod_{i=1}^{n_{\text{tr}}} \{2\pi\sigma_i^2\}^{-1/2} \right] \exp \left\{ - \sum_{i=1}^{n_{\text{tr}}} \frac{(D_i - M_i)^2}{2\sigma_i^2} \right\}, \quad (1)$$

where n_{rv} and n_{tr} are the number of RV and transit points, respectively, σ_i is the error associated to each data point D_i , M_i is the model associated to a given D_i , and σ_j is the RV error associated to stellar jitter (see also Sect. 7.1).

The sampling method and fitted parameters are the same

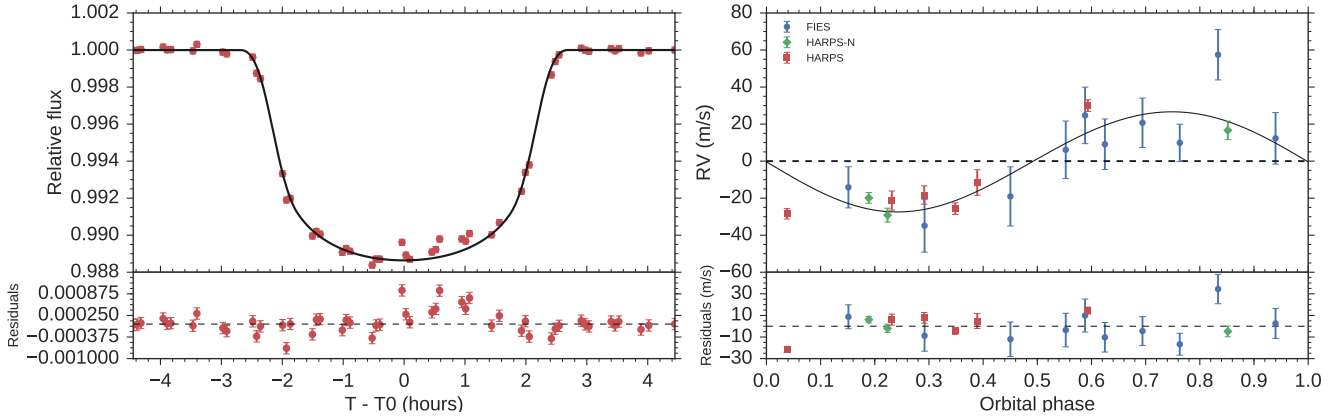


Figure 3. *Left panel:* Transit light curve folded to the orbital period of C7_6923b and residuals. The red points mark the binned *K2* data and their error bars. The solid line mark the re-binned best-fitting transit model. *Right panel:* Phase-folded FIES (blue circles), HARPS-N (green diamonds) and HARPS (red triangles) RV measurements of C7_6923 and best fitting orbit (solid line), following the subtraction of the systemic velocities as measured from each instrument. The error bars have not been corrected by the stellar jitter

as in Barragán et al. (2016). The joint modeling was performed running 500 independent chains with uniform uninformative priors in the wide ranges $P_{\text{orb}} = [28.36, 28.39]$ days, $T_0 = [2457145.7, 2457146.3]$ BJD_{TDB}, $b = [0, 1]$, $a/R_{\star} = [5, 100]$, $R_p/R_{\star} = [0, 1]$, $K = [0, 1]$ km s⁻¹, and $\gamma_j = [-32, -30]$ km s⁻¹. We fitted both circular and eccentric orbits. For the eccentricity and angle of periastron we used the parametrisation $\sqrt{e} \sin \omega$ and $\sqrt{e} \cos \omega$; for the circular model we set both parameters equal to zero, whereas for the eccentric model we set uniform uninformative priors in the range $[-1, 1]$ for the former and $[-\sqrt{1 - e \sin^2 \omega}, \sqrt{1 - e \sin^2 \omega}]$ for the latter. For the limb darkening parametrisation q_1 and q_2 (Kipping 2013) we set uniform uninformative priors in the range $[0, 1]$. We integrated over 10 steps to account for the *K2* long-cadence data. The chain convergence was analyzed using the Gelman-Rubin statistics. The burn-in phase uses 25,000 more iterations with a thin factor of 50. The posterior distribution of each parameter has 250,000 independent data points.

7 RESULTS AND DISCUSSION

The parameter estimates and their error bars – as derived using a circular model – are listed in Table 4. They are defined as the median and the 68% credible interval of the final posterior distributions. The best fitting transit and RV circular models are displayed in Figure 3 along with the photometric and RV data points.

7.1 RV jitter and spot-crossing events

Activity-induced RV jitter is expected given the 2% photometric variability observed in the light curve of C7_6923 (Fig. 1) and the emission components detected in the cores of the Ca II H & K lines. In order to account for the activity-induced RV variation, we treated the RV jitter as an extra noise in the equation of the likelihood (Eq. 1). For a fit with no jitter term the reduced chi-squared is $\chi^2_{\text{reduced}} \equiv \chi^2/\text{dof} = 7.8$. We found that a stellar jitter of $\sigma_j = 10.5 \pm 1.8$ m s⁻¹ is needed in order to obtain $\chi^2_{\text{reduced}} \approx 1$. In order to assess the goodness of our finding, we used the code SOAP2 (Dumusque et al. 2014) to estimate the expected RV variation given the rotation period of the star of 17.3 days and the 2%

observed photometric variability. Assuming that the spots are close to the stellar equator, we estimated an activity-induced RV jitter of 10–15 m s⁻¹, which is consistent with the jitter obtained from the MCMC analysis.

The passage of a planet in front of a spot can be detected as a bump in the transit light curve (see, e.g., Sanchis-Ojeda & Winn 2011). Spot-crossings events are clearly visible in the EVEREST transit light curves (Fig. 3). The same features appear at the same times and with consistent amplitudes in the Vanderburg & Johnson (2014) data, confirming that the bumps are real and not due to systematics. To assess whether the bumps significantly affect the parameter estimates, we performed the joint analysis as described in Sect 6 including all the transit data points. We found that the final parameters are consistent within 1- σ with those reported in Table 4.

7.2 Orbit eccentricity

When fitting for an eccentric orbit without accounting for the stellar jitter, we found an eccentricity of $e = 0.17^{+0.04}_{-0.03}$. When fitting for a non-circular orbit taking into account the stellar jitter (Sect. 7.1), we obtained a small non-zero eccentricity of $0.086^{+0.116}_{-0.064}$, which is not significant, implying that the best-fitting eccentric solution is driven by the RV jitter associated to the magnetic activity of the star. A quantitative way to compare the goodness of both fits is provided by the maximum likelihood and the Bayesian information criterion (BIC). The circular and eccentric fits provide a $\ln \mathcal{L}$ of 56 and 56, while the BIC favors the circular fit (BIC = -685) over the eccentric one (BIC = -675). This means that the eccentric fit does not significantly improve the fit of our data. We concluded that we are not able to measure the orbit eccentricity from our RV data and assumed a circular orbit. We stress that imposing a circular orbit have negligible effects on the values of the derived parameters of the system.

7.3 Additional companion

Huang et al. (2016) found that warm Jupiters with low eccentricities ($e \lesssim 0.4$) have inner low-mass companions. They used this evidence as an argument in favour of the *in situ* formation, since the planet migration would have cleaned the warm Jupiter neighborhood. We searched the light curve for additional transit signals

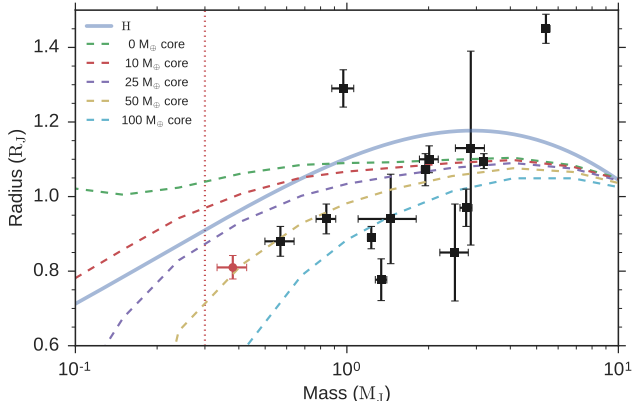


Figure 4. Warm Jupiters (black squares; $M_p \geq 0.3 M_{\text{Jup}}$ and $10 \leq P_{\text{orb}} \leq 100$ days) whose mass and radius have been estimated with a precision of at least 25% (as of January 2017, exoplanet.eu). C7_6923b is shown with a filled red circle. The solid line corresponds to a planet with a pure hydrogen composition (Seager et al. 2007). The dashed lines represent the Fortney et al. (2007) models for planet core masses of 0, 10, 25, 50 and $100 M_{\oplus}$. The vertical dotted line marks the giant planet lower limit as defined by Hatzes & Rauer (2015).

but found no evidence for an additional transiting planet in the system. The generalized Lomb-Scargle periodogram (Zechmeister & Kürster 2009) of the RV residuals show also no significant peaks.

We searched for evidence of an outer companion in the FIES, HARPS, and HARPS-N RV measurements by adding an extra linear trend $\dot{\gamma}$ to the Keplerian model fitted to the RV data (e.g., Montet et al. 2014; Smith et al. 2017). The best fit solution for the linear trend is $\dot{\gamma} = -0.37 \pm 0.13 \text{ m s}^{-1} \text{ d}^{-1}$. The $\ln \mathcal{L}$ and BIC of the models with and without linear trend are 58 and -685 , and 56 and -685 , respectively. Therefore, the model without linear trend is favored. We conclude that the currently available RV data do not provide us with significant evidence of the presence of an outer companion.

7.4 Planet’s composition and formation scenario

With a mass of $M_p = 0.381 \pm 0.045 M_{\text{Jup}}$ and radius of $R_p = 0.812 \pm 0.030 R_{\text{Jup}}$ (resulting in a mean density of $\rho_p = 0.88 \pm 0.14 \text{ g cm}^{-3}$), C7_6923b joins the small group of well characterized warm Jupiters. Fig. 4 shows the position of C7_6923b in the mass-radius diagram for warm Jupiters ($M_p \geq 0.3 M_{\text{Jup}}$; $10 \leq P_{\text{orb}} \leq 100$ days) whose mass and radius have been determined with a precision better than 25% (14 objects). Notably, C7_6923b is the transiting warm Jupiter with the lowest mass known to date, if the definition of giant planets given by Hatzes & Rauer (2015) is adopted. Fig. 4 displays also the planetary models of Fortney et al. (2007) for different core masses and age between 1.0 and 4.5 Gyrs. The planet radius of C7_6923b can be explained if the planet has a core⁵ of $48 \pm 14 M_{\oplus}$, containing $\sim 40\%$ of the total planetary mass. We expect that C7_6923b has a solid core surrounded by a gaseous envelope.

Rafikov (2006) found that a core of mass $5 - 20 M_{\oplus}$ at a semi-major axis between 0.1 and 1.0 AU would be able to start the runaway accretion phase to form a gas giant planet *in situ*. However, according to his models, these kind of cores are unlikely to form, owing to the high irradiation coming from the star. Boley et al.

(2016) suggested instead that more massive cores ($M_{\text{core}} \geq 20 M_{\oplus}$) can be built up from the merging of tightly packed inner planets (STIPs) formed at the early stages of the circumstellar disc. Batygin et al. (2016) found a similar result and argued that the massive core of HD 149026b ($M_{\text{core}} \approx 100 M_{\oplus}$) could be explained by one or more super-Earths which merged and accreted the surrounding gas to form a gas-giant planet. Huang et al. (2016) suggested that these cores can initiate runaway accretion if they are formed in a region with enough gas around them, while those without enough volatiles remain super-Earths and represent the population of massive rocky planets unveiled by *Kepler* around solar-like stars (e.g., Demory 2014). Based on these studies and given the semi-major axis of $0.1811 \pm 0.0085 \text{ AU}$, the $48 \pm 14 M_{\oplus}$ core of C7_6923b could have formed the planet *in situ*. We note that the metallicity of C7_6923 is relatively high ($[\text{Fe}/\text{H}] = 0.21 \pm 0.05$), suggesting that the primordial circumstellar disc had a relatively high content of dust, which would have enhanced the formation of the core of C7_6923b (see, e.g. Johnson & Li 2012). Alternatively, the planet might have formed beyond the snow line and migrated inwards via planet-disc interaction (see, e.g., Baruteau et al. 2014).

8 CONCLUSIONS

We confirmed the planetary nature and derived the orbital and main physical parameters of C7_6923b, a warm Jupiter ($T_{\text{eq}} = 555 \pm 11 \text{ K}$) transiting an active ($\log R'_{\text{HK}} = -4.49 \pm 0.03$) K0 V star every 29 days. We measured a planetary mass of $M_p = 0.381 \pm 0.045 M_{\text{Jup}}$ and radius of $R_p = 0.812 \pm 0.030 R_{\text{Jup}}$. At a separation of $a_p = 0.1811 \pm 0.0085 \text{ AU}$, the mean density of $\rho_p = 0.88 \pm 0.14 \text{ g cm}^{-3}$ implies that the planet has a core of $48 \pm 14 M_{\oplus}$ according to the evolutionary models of Fortney et al. (2007). C7_6923b joins the small group of well-characterized warm Jupiters whose mass and radius have been determined with a precision better than 25%.

The spin-orbit angle, i.e., the angle between the spin axis of the star and the angular momentum vector of the orbit, can provide us with valuable information on the migration mechanisms of exoplanets (see, e.g. Winn 2010; Morton & Johnson 2011; Albrecht et al. 2012; Gandolfi et al. 2012). Currently, there are only 4 warm Jupiters ($M_p \geq 0.3 M_{\text{Jup}}$ and $10 \leq P_{\text{orb}} \leq 100$ days) with measured obliquity⁶. From this perspective, C7_6923 is an ideal target to measure the sky-project spin-orbit angle via observations of the Rossiter-McLaughlin (RM) effect. Assuming spin-orbit alignment, the expected amplitude of the RM anomaly is $\Delta \text{RV} \approx \sqrt{1 - b^2} (R_p/R_*)^2 v \sin i_* \approx 25 \text{ m s}^{-1}$ (Winn 2010). Given the brightness of the host star ($V = 11.653 \text{ mag}$), this amplitude can easily be measured using state-of-the-art spectrographs such as HARPS@ESO-3.6m. Moreover, the transit duration (~ 5 hours) is shorter than the visibility of C7_6923, which is ~ 9 hours from La Silla observatory (altitude higher than 30° above the horizon).

Alternatively, the spin-orbit angle could be measured from the analysis of the spot-crossing events as described in Sanchis-Ojeda et al. (2011) and Sanchis-Ojeda et al. (2012). Anomalies ascribable to the passage of C7_6923b in front of stellar spots are visible in the 3 transit light curves observed by *K2*. Unfortunately, the limited number of transits and the *K2* long cadence data do not allow us to perform a meaningful quantitative analysis of the spot-crossing events. Given the amplitude of the detected anomalies ($\sim 0.1\%$), space-based high-precision photometry is needed to

⁵ Calculated by interpolating Fortney et al. (2007)’s model.

⁶ Source: http://www2.mps.mpg.de/homes/heller/content/main_HRM.html, as of January 2017.

detect the spot-crossing events. Observations performed with the upcoming CHaracterising ExOPlanets Satellite (CHEOPS; Broeg et al. 2013) would allow us to photometrically determine the spin-orbit angle of this system.

It is worth noting that the rotation period ($P_{\text{rot}} = 17.24 \pm 0.12$ days) and radius ($R_{\star} = 0.860 \pm 0.031 R_{\odot}$) of the host star translate into a maximum value for the projected rotational velocity of $v \sin i_{\star, \text{max}} = 2.52 \pm 0.10 \text{ km s}^{-1}$, which agrees with the spectroscopically derived $v \sin i_{\star} = 2.91 \pm 0.38 \text{ km s}^{-1}$, suggesting that the star is seen nearly equator-on ($i_{\star} \approx 90^{\circ}$) and that the system might be aligned along the line-of-sight.

ACKNOWLEDGEMENTS

We warmly thank the NOT, ESO, TNG staff members for their unique support during the observations. We are very thankful to Xavier Bonfils, François Bouchy, Martin Kürster, Tsevi Mazeh, Jorge Melendez, and Nuno Santos who kindly agreed to exchange HARPS and FIES time with us. Special thanks go to Antonino Lanza for assisting us with the calculation of the gyro-age of the star. Sz. Csizmadia thanks the Hungarian OTKA Grant K113117. H. Deeg and D. Nespral acknowledge support by grant ESP2015-65712-C5-4-R of the Spanish Secretary of State for R& D&I (MINECO). This research was supported by the Ministerio de Economía y Competitividad under project FIS2012-31079. The research leading to these results has received funding from the European Union Seventh Framework Programme (FP7/2013-2016) under grant agreement No. 312430 (OPTICON). Based on observations obtained *a*) with the Nordic Optical Telescope (NOT), operated on the island of La Palma jointly by Denmark, Finland, Iceland, Norway, and Sweden, in the Spanish Observatorio del Roque de los Muchachos (ORM) of the Instituto de Astrofísica de Canarias (IAC); *b*) with the Italian Telescopio Nazionale Galileo (TNG) also operated at the ORM (IAC) on the island of La Palma by the INAF - Fundación Galileo Galilei; *c*) the 3.6m ESO telescope at La Silla Observatory under programme ID 097.C-0948. The data presented here were obtained in part with ALFOSC, which is provided by the Instituto de Astrofísica de Andalucía (IAA) under a joint agreement with the University of Copenhagen and NOTSA. This paper includes data collected by the Kepler mission. Funding for the Kepler mission is provided by the NASA Science Mission directorate. Some of the data presented in this paper were obtained from the Mikulski Archive for Space Telescopes (MAST). STScI is operated by the Association of Universities for Research in Astronomy, Inc., under NASA contract NAS5-26555. Support for MAST for non-HST data is provided by the NASA Office of Space Science via grant NNX09AF08G and by other grants and contracts. M.F. and C.M.P. acknowledge generous support from the Swedish National Space Board. C. Eiroa and I. Rebollido are supported by Spanish grant AYA2014-55840-P. P.D. acknowledge the support from INAF and Ministero dell’Istruzione, dell’Università e della Ricerca (MIUR) in the form of the grant “Premiale VLT 2012” and “The Chemical and Dynamical Evolution of the Milky Way and Local Group Galaxies”. This work has made use of data from the European Space Agency (ESA) mission *Gaia* (<http://www.cosmos.esa.int/gaia>), processed by the *Gaia* Data Processing and Analysis Consortium (DPAC, <http://www.cosmos.esa.int/web/gaia/dpac/consortium>). Funding for the DPAC has been provided by national institutions, in particular the institutions participating in the *Gaia* Multilateral Agreement.

REFERENCES

- Albrecht S., et al., 2012, *ApJ*, **757**, 18
- Allard F., Homeier D., Freytag B., 2011, in Johns-Krull C., Browning M. K., West A. A., eds, *Astronomical Society of the Pacific Conference Series* Vol. 448, 16th Cambridge Workshop on Cool Stars, Stellar Systems, and the Sun. p. 91 ([arXiv:1011.5405](https://arxiv.org/abs/1011.5405))
- Antonini F., Hamers A. S., Lithwick Y., 2016, preprint, ([arXiv:1604.01781](https://arxiv.org/abs/1604.01781))
- Barnes S. A., 2010, *ApJ*, **722**, 222
- Barnes S. A., Kim Y.-C., 2010, *ApJ*, **721**, 675
- Barragán O., et al., 2016, *AJ*, **152**, 193
- Baruteau C., et al., 2014, *Protostars and Planets VI*, pp 667–689
- Batygin K., Bodenheimer P. H., Laughlin G. P., 2016, *ApJ*, **829**, 114
- Boley A. C., Granados Contreras A. P., Gladman B., 2016, *ApJ*, **817**, L17
- Brahm R., et al., 2016, *AJ*, **151**, 89
- Bressan A., Marigo P., Girardi L., Salasnich B., Dal Cero C., Rubele S., Nanni A., 2012, *MNRAS*, **427**, 127
- Broeg C., et al., 2013, in *European Physical Journal Web of Conferences*. p. 03005 ([arXiv:1305.2270](https://arxiv.org/abs/1305.2270)), doi:10.1051/epjconf/20134703005
- Bruntt H., et al., 2010, *MNRAS*, **405**, 1907
- Buchhave L. A., et al., 2010, *ApJ*, **720**, 1118
- Cabrera J., et al., 2009, *A&A*, **506**, 501
- Cabrera J., Csizmadia S., Erikson A., Rauer H., KIRSTE S., 2012, *A&A*, **548**, A44
- Cabrera J., et al., 2014, *ApJ*, **781**, 18
- Cantat-Gaudin T., et al., 2014, *A&A*, **562**, A10
- Cardelli J. A., Clayton G. C., Mathis J. S., 1989, *ApJ*, **345**, 245
- Carone L., et al., 2012, *A&A*, **538**, A112
- Carpano S., et al., 2009, *A&A*, **506**, 491
- Castelli F., Kurucz R. L., 2004, preprint,
- Cavarroc C., et al., 2012, *Ap&SS*, **337**, 511
- Chabrier G., 2001, *ApJ*, **554**, 1274
- Cosentino R., et al., 2012, in *Ground-based and Airborne Instrumentation for Astronomy IV*. p. 84461V, doi:10.1117/12.925738
- Cutri R. M., et al., 2003, *2MASS All Sky Catalog of point sources*.
- Cutri R. M., et al., 2012, Technical report, Explanatory Supplement to the WISE All-Sky Data Release Products
- Dawson R. I., Johnson J. A., Morton T. D., Crepp J. R., Fabrycky D. C., Murray-Clay R. A., Howard A. W., 2012, *ApJ*, **761**, 163
- Demory B.-O., 2014, *ApJ*, **789**, L20
- Dong S., Katz B., Socrates A., 2014, *ApJ*, **781**, L5
- Doyle A. P., Davies G. R., Smalley B., Chaplin W. J., Elsworth Y., 2014, *MNRAS*, **444**, 3592
- Dumusque X., Boisse I., Santos N. C., 2014, *ApJ*, **796**, 132
- Endl M., Cochran W. D., 2016, *PASP*, **128**, 094502
- Erikson A., et al., 2012, *A&A*, **539**, A14
- Fabrizius C., et al., 2016, *A&A*, **595**, A3
- Fortney J. J., Marley M. S., Barnes J. W., 2007, *ApJ*, **659**, 1661
- Fossati et al. 2017, *A&A*, submitted
- Frandsen S., Lindberg B., 1999, in Karttunen H., Piirola V., eds, *Astrophysics with the NOT*. p. 71
- Frewen S. F. N., Hansen B. M. S., 2016, *MNRAS*, **455**, 1538
- Gandolfi D., et al., 2008, *ApJ*, **687**, 1303
- Gandolfi D., et al., 2012, *A&A*, **543**, L5
- Gandolfi D., et al., 2015, *A&A*, **576**, A11
- Grziwa S., Pätzold M., 2016, preprint, ([arXiv:1607.08417](https://arxiv.org/abs/1607.08417))
- Grziwa S., Pätzold M., Carone L., 2012, *MNRAS*, **420**, 1045
- Hamers A. S., Antonini F., Lithwick Y., Perets H. B., Portegies Zwart S. F., 2016, preprint, ([arXiv:1606.07438](https://arxiv.org/abs/1606.07438))
- Hatzes A. P., Rauer H., 2015, *ApJ*, **810**, L25
- Heiter U., et al., 2015, *Phys. Scr.*, **90**, 054010
- Huang C., Wu Y., Triaud A. H. M. J., 2016, *ApJ*, **825**, 98
- Johnson J. L., Li H., 2012, *ApJ*, **751**, 81
- Kipping D. M., 2013, *MNRAS*, **435**, 2152
- Kley W., Nelson R. P., 2012, *ARA&A*, **50**, 211
- Kovács G., Zucker S., Mazeh T., 2002, *A&A*, **391**, 369

Table 4. System parameters.

Parameters	Values
<i>Model Parameters</i>	
Orbital period P_{orb} (days)	28.38229 ± 0.00027
Transit epoch T_0 (BJD _{TDB} -2 450 000)	7325.81705 ± 0.00033
Scaled semi-major axis a/R_{\star}	$45.3^{+1.3}_{-1.5}$
Scaled planet radius R_p/R_{\star}	$0.0970^{+0.0013}_{-0.0012}$
Impact parameter, b	$0.352^{+0.083}_{-0.097}$
Eccentricity ^(a) e	0
Parameterized limb-darkening coefficient q_1	0.46 ± 0.10
Parameterized limb-darkening coefficient q_2	0.33 ± 0.09
Radial velocity semi-amplitude variation K (m s^{-1})	26.9 ± 3.2
Systemic velocity γ_{FIES} (km s^{-1})	-31.3566 ± 0.0039
Systemic velocity γ_{HARPS} (km s^{-1})	-31.1925 ± 0.0036
Systemic velocity $\gamma_{\text{HARPS-N}}$ (km s^{-1})	-31.1857 ± 0.0046
Stellar jitter σ_j (m s^{-1})	10.5 ± 1.8
<i>Derived parameters</i>	
Semi-major axis of the planetary orbit a (AU)	0.1811 ± 0.0085
Orbit inclination along the line-of-sight i_p ($^{\circ}$)	$89.55^{+0.13}_{-0.12}$
Linear limb-darkening coefficient u_1	0.44 ± 0.07
Quadratic limb-darkening coefficient u_2	0.24 ± 0.14
Transit duration τ_{14} (hours)	4.966 ± 0.036
Transit ingress/egress duration $\tau_{12} = \tau_{34}$ (hours)	0.496 ± 0.035
<i>Stellar parameters</i>	
Effective Temperature T_{eff} (K)	5287 ± 60
Surface gravity ^(b) $\log g_{\star}$ (cgs)	4.52 ± 0.06
Surface gravity ^(c) $\log g_{\star}$ (cgs)	4.504 ± 0.035
Iron abundance [Fe/H] (dex)	0.21 ± 0.05
Microturbulent velocity v_{mic} (km s^{-1})	0.87 ± 0.06
Macroturbulent velocity v_{mac} (km s^{-1})	2.44 ± 0.38
Projected rotational velocity $v \sin i_{\star}$ (km s^{-1})	2.91 ± 0.38
Rotational period P_{rot} (days)	17.24 ± 0.12
Star mass M_{\star} (M_{\odot})	0.918 ± 0.028
Star radius R_{\star} (R_{\odot})	0.860 ± 0.031
Star density ρ_{\star} (g cm^{-3})	2.19 ± 0.20
Gyrochronological age (Gyr)	1.8 ± 0.3
Interstellar extinction A_V (mag)	0.05 ± 0.05
Star distance ^(d) d (pc)	152 ± 10
<i>Planetary parameters</i>	
Planet mass M_p (M_{Jup})	0.381 ± 0.045
Planet radius R_p (R_{Jup})	0.812 ± 0.030
Planet density ρ_p (g cm^{-3})	0.88 ± 0.14
Equilibrium temperature ^(e) T_{eq} (K)	555 ± 11

Note – ^(a) Fixed. ^(b) As derived from the spectral analysis. ^(c) As derived from the PARSEC model isochrones (Bressan et al. 2012), using the *Gaia*'s parallax, the EPIC visual magnitude, along with the effective temperature (T_{eff}), iron content ([Fe/H]), and interstellar extinction (A_V) derived in this work. ^(d) From the *Gaia*'s first data release (Fabricius et al. 2016). ^(e) Assuming zero albedo and uniform planetary energy redistribution.

Kurucz R. L., 2013, ATLAS12: Opacity sampling model atmosphere program, Astrophysics Source Code Library (ascl:1303.024)
 Luger R., Agol E., Kruse E., Barnes R., Becker A., Foreman-Mackey D., Deming D., 2016, *AJ*, **152**, 100
 Magrini L., et al., 2013, *A&A*, **558**, A38
 Mandel K., Agol E., 2002, *ApJ*, **580**, L171
 Mayor M., et al., 2003, *The Messenger*, **114**, 20
 McQuillan A., Mazeh T., Aigrain S., 2014, *ApJS*, **211**, 24
 Montet B. T., Crepp J. R., Johnson J. A., Howard A. W., Marcy G. W., 2014, *ApJ*, **781**, 28
 Morton T. D., Johnson J. A., 2011, *ApJ*, **729**, 138
 Niedzielski A., et al., 2016, preprint, (arXiv:1603.07581)
 Ortiz M., et al., 2015, *A&A*, **573**, L6
 Pecauc M. J., Mamajek E. E., 2013, *ApJS*, **208**, 9

Petrovich C., Tremaine S., 2016, preprint, (arXiv:1604.00010)
 Rafikov R. R., 2006, *ApJ*, **648**, 666
 Ryabchikova T. A., Pakhomov Y. V., Piskunov N. E., 2011, *Kazan Izdatel Kazanskogo Universiteta*, **153**, 61
 Sanchis-Ojeda R., Winn J. N., 2011, *ApJ*, **743**, 61
 Sanchis-Ojeda R., Winn J. N., Holman M. J., Carter J. A., Osip D. J., Fuentes C. I., 2011, *ApJ*, **733**, 127
 Sanchis-Ojeda R., et al., 2012, *Nature*, **487**, 449
 Schlegel D. J., Finkbeiner D. P., Davis M., 1998, *ApJ*, **500**, 525
 Seager S., Kuchner M., Hier-Majumder C. A., Militzer B., 2007, *ApJ*, **669**, 1279
 Smith A. M. S., et al., 2017, *MNRAS*, **464**, 2708
 Sneden C., Bean J., Ivans I., Lucatello S., Sobeck J., 2012, MOOG: LTE line analysis and spectrum synthesis, Astrophysics Source Code Li-

- brary (ascl:1202.009)
Stetson P. B., Pancino E., 2008, *PASP*, **120**, 1332
Telting J. H., et al., 2014, *Astronomische Nachrichten*, **335**, 41
Tull R. G., MacQueen P. J., Sneden C., Lambert D. L., 1995, *PASP*, **107**, 251
Valenti J. A., Fischer D. A., 2005, *ApJS*, **159**, 141
Valenti J. A., Piskunov N., 1996, *A&AS*, **118**, 595
Vanderburg A., Johnson J. A., 2014, *PASP*, **126**, 948
Winn J. N., 2010, *Exoplanet Transits and Occultations*. University of Arizona Press, pp 55–77
Zechmeister M., Kürster M., 2009, *A&A*, **496**, 577
da Silva L., et al., 2006, *A&A*, **458**, 609

This paper has been typeset from a \TeX/L\AA\TeX file prepared by the author.